Physical properties of gneiss and amphibolite in central west Greenland: Implications for thermal regime in permafrost

OLE SKURSCH, ERMIS PROESTAKIS & THOMAS INGEMAN-NIELSEN

Skursch, O., Proestakis, E. & Ingeman-Nielsen, T. 2026. Physical properties of gneiss and amphibolite in central west Greenland: Implications for thermal regime in permafrost. Bulletin of the Geological Society of Denmark, Vol. 75, pp. 263–281. ISSN 2245-7070. https://doi.org/10.37570/bgsd-2026-75-14

Geological Society of Denmark
https://2dgf.dk

Received 27 July 2026
Accepted in revised form 2 October 2026
Published online 28 October 2026

© 2026 the authors. Re-use of material is permitted, provided this work is cited. Creative Commons License CC BY: https://creativecommons.org/licenses/by/4.0/

Understanding the ground thermal regime in permafrost regions is important because seasonal and climatic temperature variations are related to human risks. Small local variations in the ground thermal regime can be accelerated by positive feedback loops leading to accelerated permafrost degradation. In central West Greenland, we hypothesize that mafic Kangâmiut dykes and their gneissic host rocks have contrasting thermal properties, and that it can lead to differences in the ground thermal regime across very small distances. To test this, we measure the thermal properties of gneiss and a Kangâmiut dyke as well as minor pegmatite and supracrustal rock in a drill core (GIOS2023-01) near Kangerlussuaq. Temperature measurements from the corresponding borehole allow us to calculate a local heat flux of 48 ± 4 to 51 ± 4 mW m^{-2}. To understand the thermal conductivity under *in situ* conditions, we use ultrasonic P- and S-wave velocity as a proxy to evaluate its dependence on pore fluid and lithostatic pressure. Together, thermal properties and heat flux provide input to transient numerical thermal models that explore the ground thermal regime under different scenarios. The thermal properties of the gneiss (k = 3.1–3.4 W m^{-1} K^{-1}, ϱ = 2603–2703 kg m^{-3}, c_p = 754–825 J kg^{-1} K^{-1}) is clearly different from those of the amphibolitic dyke (k = 2.5–4.6 W m^{-1} K^{-1}, ϱ = 3049–3088 kg m^{-3}, c_p = 660–672 J kg^{-1} K^{-1}). One supracrustal sample (k = 3.03 W m^{-1} K^{-1}, ϱ = 2926 kg m^{-3}, c_p = 695 J kg^{-1} K^{-1}) is somewhat similar to the dyke, whereas a quartz-rich pegmatite is highly conductive (k = 6.9 W m^{-1} K^{-1}, ϱ = 2622 kg m^{-3}, c_p = 893 J kg^{-1} K^{-1}). Although ultrasonic velocities indicate that elastic moduli increase with axial stress and vary between gneiss and dyke, and between wet and dry state, these mechanical effects translate into negligible changes in thermal conductivity. For exposed bedrock, transient numerical thermal models suggest that the active layer thickness is several decimetres thicker in gneiss than in the dyke, and that the difference is in the order of metres when comparing gneiss or dyke to the pegmatite. With increasing sediment thickness overlying the bedrock, the difference in active layer thickness decreases. At a certain sediment thickness (~0.75 m with the chosen sediment properties), the active layers thicknesses reverse, i.e. active layers in the dyke are thicker than in gneiss (and pegmatite). This shift reflects two opposite effects: with no or little sediment cover, the relatively dense dyke is resistant to annual temperature variations. As sediment thickness increase, more of the temperature variations occurs in the sediment, and the dyke act as a heat sink, causing high temperature gradients and fast heat diffusion. As the sediment thickness exceeds the active layer thickness, the difference in active layer thickness between lithologies decreases to few centimetres. This small difference persists for several metres of sediment cover (~4 m with the chosen sediment properties). Metre-scale differences in active layer thickness have direct consequences for stability of rock slopes. Although centimetre-scale differences in active layer thickness will have limited influence on the stability of the sediment, it can accelerate by positive feedback loops. This insight could be validated in future field studies and provide input to predictive models of permafrost instability.

Keywords: West Greenland, Kangâmiut dyke, GIOS2023-01, thermal properties, elastic moduli, permafrost, CryoGrid.

O. Skursch [olsku@dtu.dk] and T. Ingeman-Nielsen [thin@dtu.dk] Department of Environmental and Resource Engineering, Technical University of Denmark, 2800 Kgs. Lyngby, Denmark; E. Proestakis [ermpr@dtu.dk] Danish Offshore Technology Center, Technical University of Denmark, 2800 Kgs. Lyngby, Denmark.

Understanding the ground thermal regime in permafrost regions is important because seasonal variations and climatic warming increase risks and increase physical weathering of rock. Risks to infrastructure and buildings include changes to the temperature-dependent bearing capacity of un- or partially frozen sediment (Andersland & Ladanyi 1994; Agergaard & Ingemann-Nielsen 2012) and heaving related to freezing and thawing of the active layer (Hjort *et al*. 2022). Heaving is caused by expansion related to the water-ice phase transition and can cause surface pressures up to 1800 kPa on overlying human-made structures (Penner 1970). The exact magnitude of the pressure depends, among other things, on the active layer thickness, with empirical data suggesting a positive correlation between pressure and active layer thickness (Tsytovich 1959). Other risks include active-layer detachments (McRoberts & Morgenstern 1974; Leibman 1995; Lewkowicz 2007) and debris flows (Zimmerman & Haeberli 1992; Lewkowicz & Hartshorn 1998; Sattler *et al.* 2011). Both phenomena are caused by temporarily high pore-water pressure in sediment leading to lower shear strength and downslope movement. The high pore-water pressure may be directly related to the ground thermal regime by melting of snow or pore ice, or to precipitation events (Lewkowicz *et al.* 2025). Melting may also lead to rock-slope failures (Gruber & Haeberli 2007; Vivani *et al*. 2020; Marcer *et al*. 2024) that can have catastrophic consequences (Svennevig *et al*. 2024). Finally, freeze-thaw cycles cause physical weathering of bedrock that with time weakens the rock and influence landscape evolution (Anderson 1998).

The ground thermal regime is determined by many parameters, including surface temperature, crustal heat flux, porosity and physical properties of sediment, rock and pore fluid (density, specific heat capacity, thermal conductivity, latent heat related to phase change). In sediments, the thermal regime can vary greatly over short distances as porosity changes alter physical properties (Harris *et al*. 2018, and references therein; Hrbáček *et al*. 2025). Understanding such local variations in the thermal regime is important because positive feedback loops can accelerate permafrost degradation (Devoie *et al*. 2019; Chen *et al*. 2023; Wang *et al*. 2025; Luo *et al.* 2025). This contribution investigates the influence of local variations in bedrock lithology on the thermal regime. We choose a study area in West Greenland characterized by (1) numerous recent sediment slides (Nielsen *et al.* 2026), (2) a relatively simple geological structure where rocks of contrasting physical properties are in direct contact, and (3) a specific need for understanding permafrost distribution in relation to ongoing infrastructure construction, namely the country's first intercity road connecting Kangerlussuaq to Sisimiut. For a selected drill core and corresponding borehole, we present new data on physical properties of rocks relevant for crustal heat flow. In addition, we measure P- and S-wave velocity under different stress states and use these data to calculate elastic moduli. This allows us to test for porosity variations with increas-

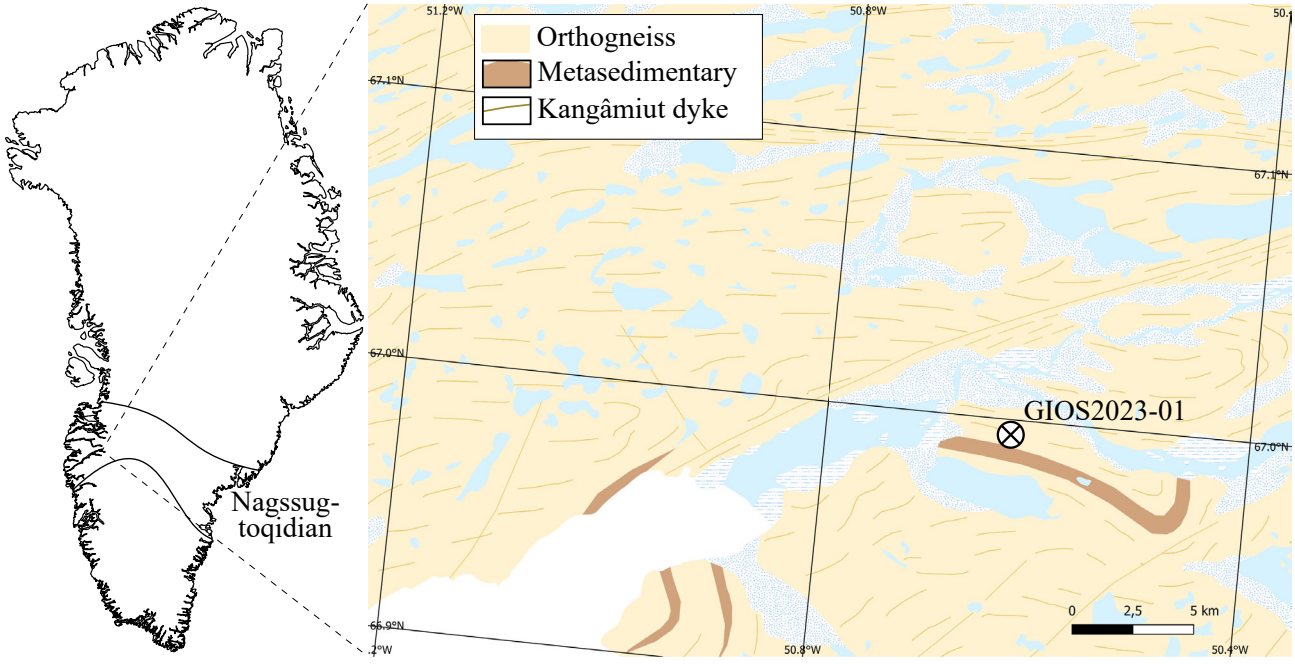


Fig. 1. Position of study area and geological map (simplified from Kokfelt *et al.* 2023) around Kangerlussuaq with position of drill core GIOS2023-01 and Nagssugtoqidian orogen indicated.

ing stress and assess how the physical properties of the rock vary with depth. Additionally, temperature measurements in the borehole are presented, allowing us to calculate the local heat flux. Heat flux measurements are known from a limited number of locations in Greenland and are important for modeling of permafrost as well as ice-sheet processes. We use the physical properties of the rock and local heat flux as inputs for finite difference numerical models that investigate how the thermal regime can vary with bedrock properties. We extend numerical modeling to situations where sediment overlie the bedrock and discuss possible implications for society.

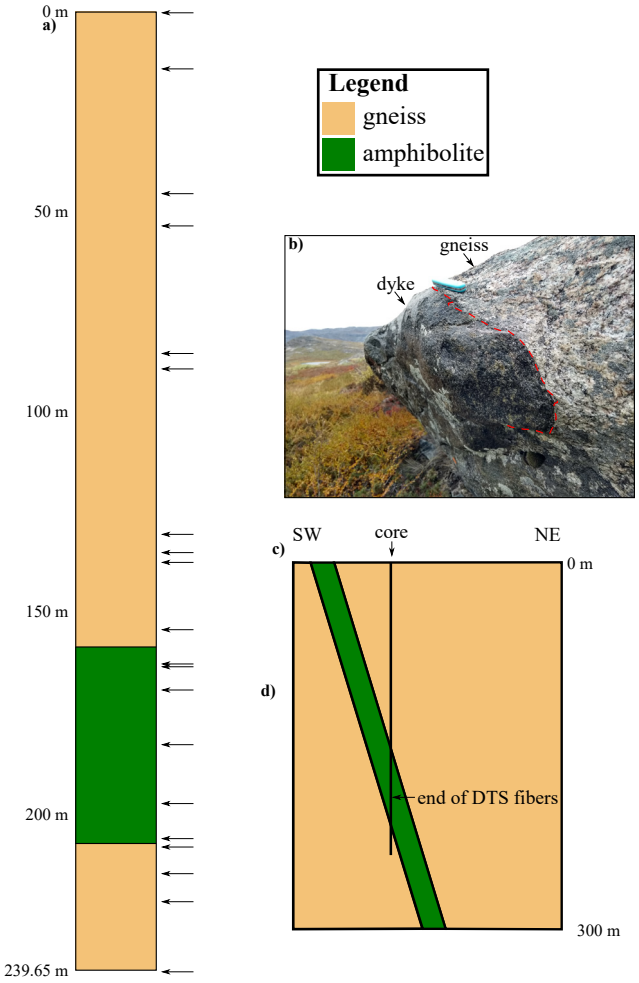


Fig. 2. a) Simplified core log, key as in Fig. 1. Arrows indicate position of samples for thin section and thermal measurements. b) Field photograph of contact between gneiss and amphibolite. c) Cross section showing orientation of the dyke, position of core and borehole, and end of DTS fibers for temperature measurements.

Background

Regional geology and permafrost distribution

The Nagssugtoqidian Orogen spans a belt in the ice-free part of West Greenland between c. 65.5 and 67°N and is dominated by high-grade metamorphic rocks (Fig. 1; van Gool *et al.* 2002). Different gneissic units dominate volumetrically over supracrustals and are intruded by the Kangâmiut dyke swarm (Fig. 1b). The structural setting and geochemical affinity of the Kangâmiut dykes suggest emplacement during passive rifting at 2040 Ma and subsequent metamorphic overprinting at granulite facies conditions during the Nagssugtoqidian at 1860–1775 Ma (Mayborn & Lesher 2006; van Gool *et al.* 2022; Korstgård *et al.* 2024; Sørensen *et al.* 2025).

The region is at present characterized by relatively mild coastal to colder continental climate. Permafrost conditions are continuous and relatively thick near the inland ice to sporadic near the coast (Obu *et al.* 2019), due to climatic variations.

Geology of the drill site and description of drill core

Drill site

The GIOS2023-01 core was drilled vertically into a flat surface of orthogneiss on a relatively flat plateau 1.5–2 km southeast of Kangerlussuaq at 175–200 m elevation. Approximately 160 metres southwest of the drill site, a Kangâmiut dyke crops out. Along the strike of the dyke, a narrow valley with relatively steep sides has developed. This valley can be traced north to a near-vertical rock face bounding the Qinnguata Kuussua (Watson River) valley. On the eastern side of the small valley, a sharp contact between dyke and gneiss is exposed (Fig. 2b), which allowed us to estimate the strike and dip of the dyke to 120/73 NE, i.e. dipping towards the drill site.

The Holocene geological history of Kangerlussuaq was summarized by Ingeman-Nielsen (2026). At the last glacial maximum, the drill site was covered by glacier ice, as evidenced by scour marks adjacent to the borehole. Retreat of the ice initiated at 12–10 ka (Lesnek *et al.*, 2020; Carlson *et al.* 2021) and the area was ice-free to an elevation of 120 metres by 8.0 ka (Levy *et al.* 2018; Carlson *et al.* 2021).

Core and borehole

Drilling operations employed NQ-size equipment, recovering 47.6 mm diameter core to a depth of 239.65 m below ground surface (m b.g.s.). The core is domi-

nated by orthogneiss, intersected by a Kangâmiut dyke between 158.76 and 207.81 m b.g.s. (Fig. 2a). The field and core observations are consistent with the dyke continuing as a tabular body from the surface downward (Fig. 2c). The gneiss has varying content of mafic minerals and foliation is best developed in mafic variants. Minor amounts of pegmatite, tens of cm thick, occur within the gneiss and are dominated by quartz and feldspar in different modal proportions. Some pegmatites are almost monomineralic and quartz-rich, others granitic, and two show concentric modal layering. The 3D structure of the pegmatites is unknown but may extend to the surface where the gneiss is cut by randomly oriented tabular bodies of pegmatite of decimetre thickness. A biotite-rich lithology likely represents a small amount of supracrustal unit embedded in the gneiss.

The borehole was instrumented with an optical DTS (distributed temperature sensing) cable to a depth of 190.7 m b.g.s. The cable contains four individual multimode fibers looped at the bottom of the hole to allow pair-wise, dual-ended temperature measurements.

Material and methods

Samples and sampling strategy

We collected 20 samples from the drill core (Fig. 2a) with lengths of ~20 cm (Table 1). Sample numbers consist of the core identifier (GIOS2023-01) combined with trailing numbers that indicate the sampling depth in metres, measured from the base of the samples.

In the gneiss, proportions of mafic minerals vary over tens of metres. Following visual logging, we sampled alternating mafic and felsic gneiss. This approach was preferred to sampling regular depth intervals because we assume that the physical properties are determined by the mineralogy and that mafic and felsic gneiss thus bracket the physical properties. We sampled the amphibolite at regular intervals although making sure to sample close to the contact.

Petrography

Petrographic observations were obtained using optical and scanning electron microscopy (SEM) on polished thin sections. Following qualitative petrographic observations, we selected one typical amphibolite sample (GIOS2023-01-169.48) and one gneiss sample (GIOS2023-01-239.44) for further analysis. To obtain mineral modes, we point counted the selected amphibolite (n = 522) and gneiss (n = 1026) and calculated the volume proportions and corresponding uncertainties following Galehouse (1971).

Table 1. Sample list, description and analyses. Trailing numbers indicate sample depth in the GIOS2023-01 core

Sample number	Description	Thermal measurements	Polished thin section	Point cointed	Ultrasonic velocities
GIOS2023-01-0.80	relatively felsic gneiss	x	x	–	–
GIOS2023-01-14.76	relatively mafic gneiss, foliated	x	x	–	–
GIOS2023-01-45.79	relatively mafic gneiss, banded	x	x	–	–
GIOS2023-01-53.65	relatively felsic gneiss, coarse-grained	x	x	–	–
GIOS2023-01-85.67	relatively mafic gneiss	x	x	–	–
GIOS2023-01-89.27	relatively felsic gneiss, coarse-grained	x	x	–	–
GIOS2023-01-130.47	gneiss, spotted with alkali feldspar	x	x	–	–
GIOS2023-01-135.28	gneiss	x	x	–	–
GIOS2023-01-137.46	biotite-rich, probably supracrustal	x	x	–	–
GIOS2023-01-154.34	relatively mafic gneiss, coarse-grained	x	x	–	–
GIOS2023-01-162.97	dyke, foliated	x	x	–	–
GIOS2023-01-163.97	dyke, foliated	x	x	–	–
GIOS2023-01-169.48	dyke, foliated	x	x	x	x
GIOS2023-01-183.14	dyke, foliated	x	x	–	–
GIOS2023-01-197.65	dyke, foliated	x	x	–	–
GIOS2023-01-206.30	dyke, foliated	x	x	–	–
GIOS2023-01-208.39	felsic gneiss	x	x	–	–
GIOS2023-01-215.09	relatively mafic gneiss	x	x	–	–
GIOS2023-01-222.00	relatively felsic gneiss, banded?	x	x	–	–
GIOS2023-01-239.44	gneiss	x	x	x	x

Thermal properties

We measured thermal conductivity (k) and effusivity (e) of 22 samples using a third-generation C-Therm TCi system (C-Therm Technologies Ltd. 2013) at room temperature, with water as contact agent. Samples were cut and split as indicated in Fig. 3, and measurements were conducted on both vertical and horizontal faces to capture potential variation in properties in the generally coarse-grained and inhomogeneous samples. We typically conducted three to four measurements per area in two to four different areas on each surface. We calibrated the system using the Pyroceram reference material provided by the manufacturer (C-THERM Technologies). The reported reference values are k = 3.967 W m^{-1} K^{-1} and e = 2950.4 W $s^{0.5}$ m^{-2} K^{-1} (C-Therm Technologies Ltd. 2013). During our testing, we obtained k = 4.09 ± 0.05 W m^{-1} K^{-1} and e = 2950 ± 22 W $s^{0.5}$ m^{-2} K^{-1} (2 standard deviations, n = 110 measurements), corresponding to an accuracy of 3 % in thermal conductivity and 0.02 % in thermal effusivity, or a precision of 1 % and 0.7 %, respectively. In comparison, the accuracy and precision is reported as better than 5% and 1%, respectively, by the manufacturer (C-Therm Technologies Ltd. 2013).

After measurements on dry samples, selected samples (GIOS2023-01-169.48 and GIOS2023-01-239.44) were water-saturated in a desiccator using a 60–230 mbar vacuum by gradually adding demineralized water until samples were fully submerged. Subsequent thermal measurements were then performed on the saturated samples. Sample porosity was calculated as the ratio of pore volume to sample volume. Pore volume was calculated gravimetrically, as the difference in mass between the dry and water-saturated (surface-dry) sample, while sample volume was based on cylindrical dimensions measured by caliper.

Some samples are not perfectly cylindrical, and their volumes could not be calculated from their cylindrical dimensions. We thus used Archimedes' principle to obtain sample volumes. For densities calculated using Archimedes' principle, we report uncertainties propagated from the balance precision (± 0.1 g), which we consider the major uncertainty contribution. Volumes calculated using Archimedes' principle and those derived from cylindrical dimensions agree to within 1% .

Specific heat capacity (c_p) and thermal diffusivity (D) were calculated as

$$c_P = \frac{e^2}{k\rho} \quad \text{and} \qquad \textit{Eq.}\ 1$$

$$\mathrm{D} = \frac{k}{\rho c_P}, \qquad \textit{Eq.}\ 2$$

where e is effusivity, k is thermal conductivity and ϱ is density.

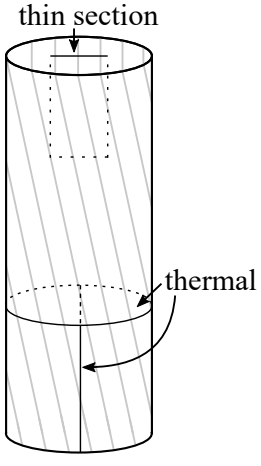


Fig. 3. Schematic illustration of how thin sections and rock slabs for thermal conductivity measurements were cut. In the rock slabs, two perpendicular surfaces were obtained. The vertical surface is close to being parallel to the foliation and the horizontal surface close to being perpendicular to foliation.

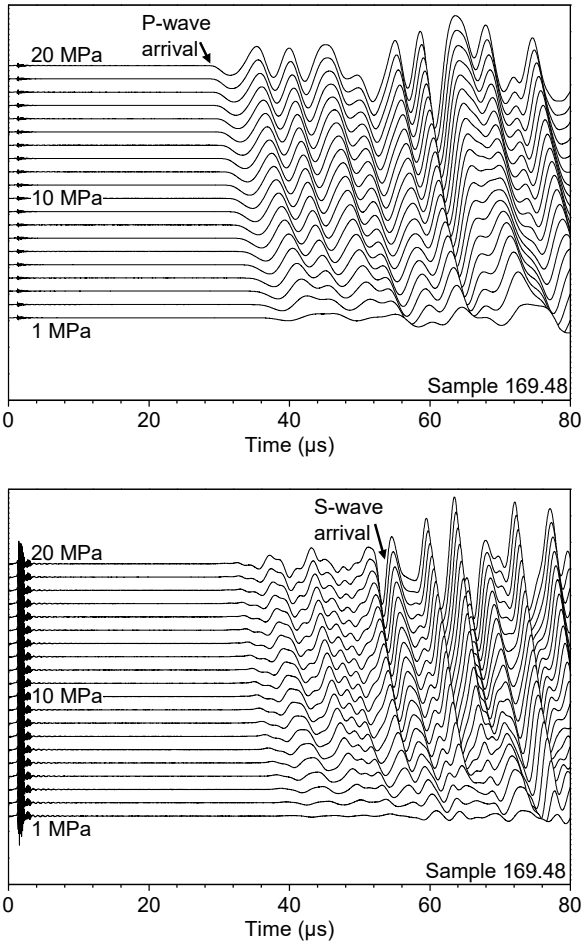


Fig. 4. P- and S-wave trains from sample 169.48 plotted against stress, incremented by 1 MPa from 1 to 20 MPa. The P-wave arrival is marked by the first deflection on the wave train. The S-wave arrival appears as a distinct amplitude spike and becomes clearer at higher stress.

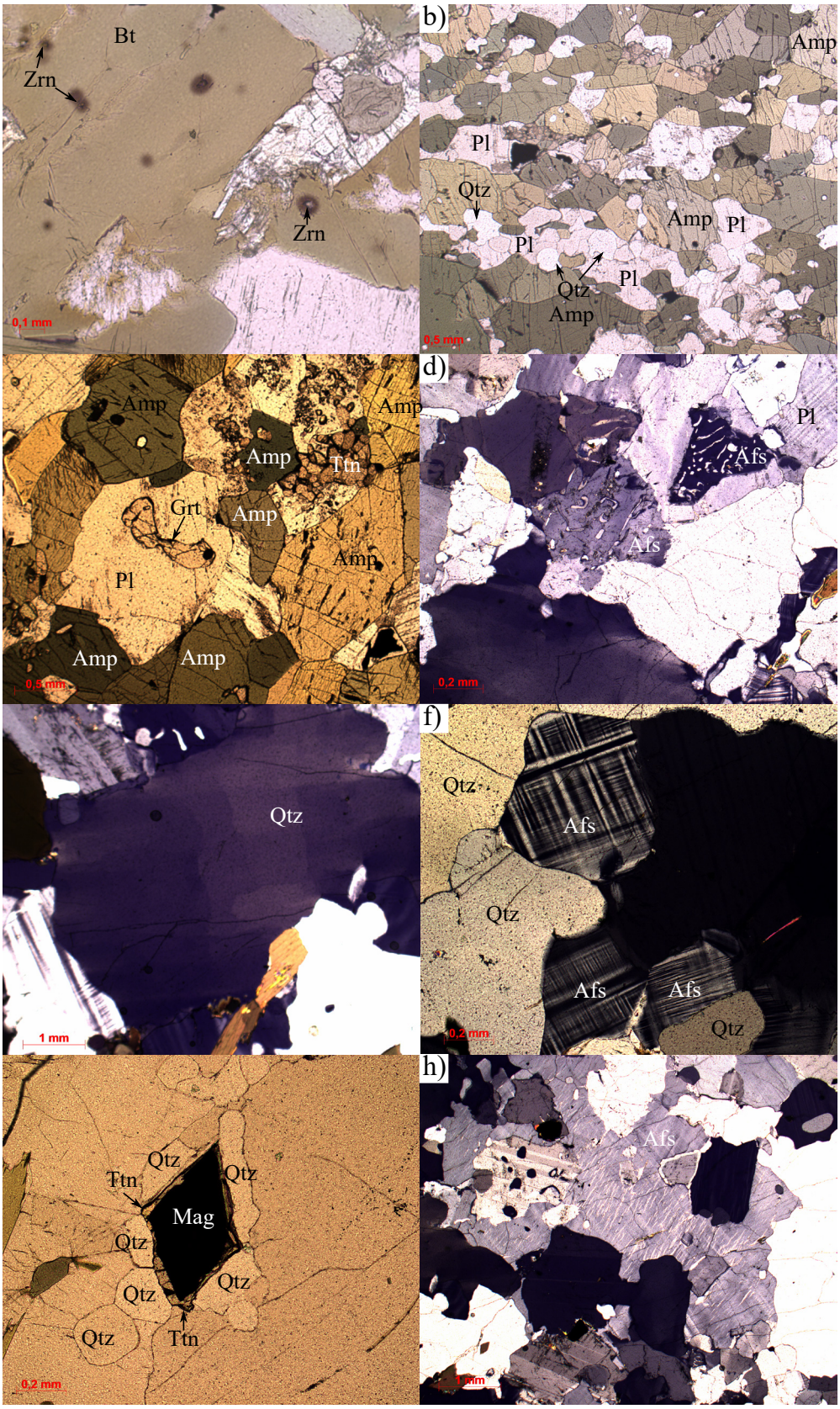


Fig. 5. Microscopic images. a) Biotite (Bt) and zircon (Zrc) in supracrustal (sample GIOS2023-01-137.46). b) Bands of yellow-green pleochroic amphibole (Amp) and colorless plagioclase (Pl) and quartz (Qtz) in sample GIOS2023-01-169.48. c) Garnet (Grt) embedded in plagioclase and titanite (Ttn) aggregate (sample GIOS2023-01-169.48). d) micrographic intergrowth between alkali feldspar (Afs) and quartz (sample GIOS2023-01-239.44). e) Quartz with undulating extinction (sample GIOS2023-01-239.44). f) Two twin orientations in alkali feldspar (sample GIOS2023-01-239.44). g) Magnetite (Mag) rimmed by titanite. h) Perthite exsolution in alkali feldspar (sample GIOS2023-01-239.44). d, e, h crossed polarizers, remaining plane polarized light.

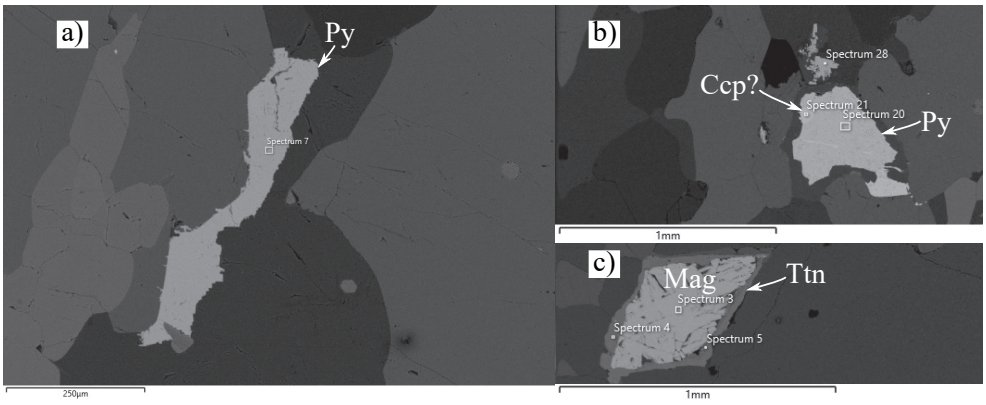


Fig. 6. Scanning electron microscopy images of polished thin sections. a) Relatively small pyrite (Py) grain isolated by silicate minerals (sample GIOS2023-01-169.48). b) Small exsolution or overgrowth of Cu-Fe sulfide (chalcopyrite?, Ccp) on pyrite (sample GIOS2023-01-169.48). c) Titanite (Ttn) rimming magnetite (Mag) (sample GIOS2023-01-239.44).

Elastic moduli and stress-strain measurements

We determined the elastic moduli at various stress states for the selected gneiss (GIOS2023-01-239.44) and amphibolite samples (GIOS2023-01-169.48) in both dry and water-saturated state. Cylindrical samples of known dimensions were mounted in a load frame, preloaded to 10 MPa and unloaded to 0.2 MPa in order to close pre-existing microfractures and improve piston-to-sample contact. Samples were then loaded incrementally to 20 MPa in steps of 1 MPa along the sample longitudinal axis and under unconfined conditions.

At each stress state, we recorded one P-wave and two orthogonal S-wave trains using piezoelectric transducers embedded within the piston heads, cali-

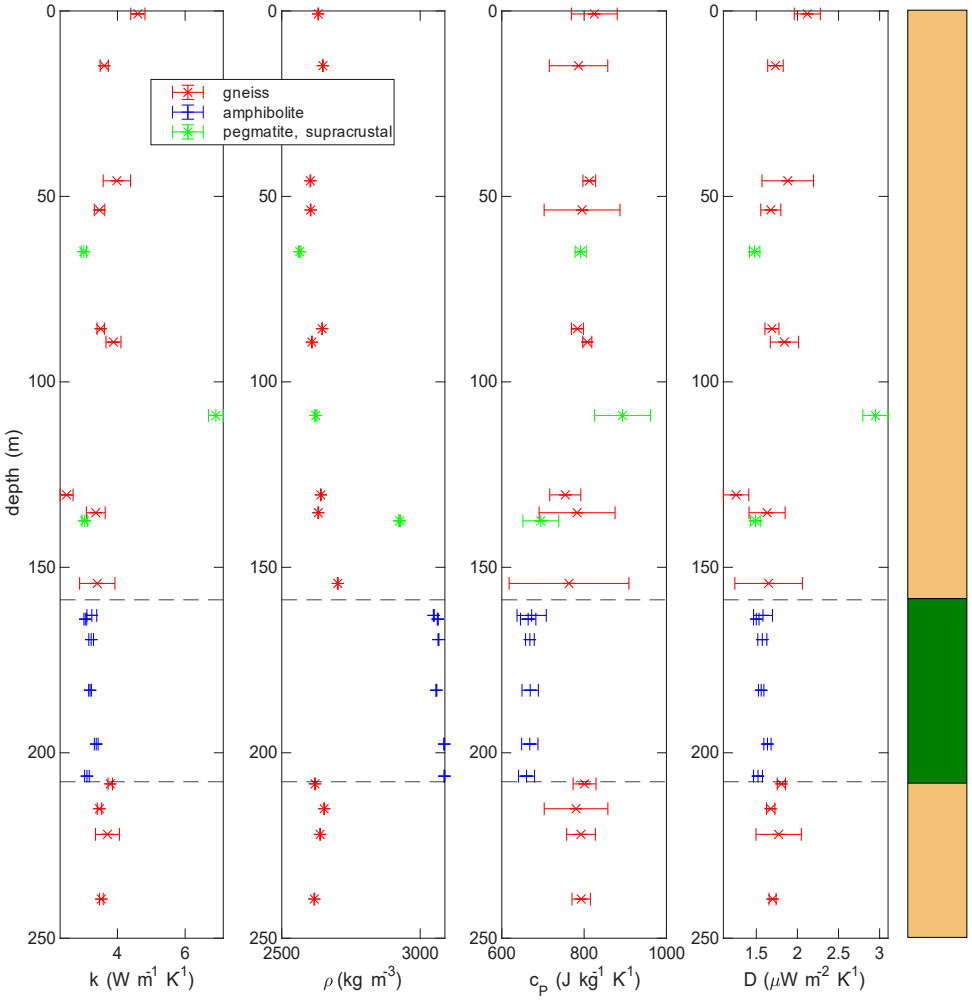


Fig. 7. Physical properties with depth in the drill core. a) Thermal conductivity in the vertical direction, b) density, c) specific heat capacity (calculated using Eq. 1), d) diffusivity. Also shown is the simplified lithological log. c-d calculated from vertical measurements of conductivity and effusivity. Error bars are 2 s.d.

brated for system dead time. The resonant frequency of the P and S-wave crystals was around 150 kHz. From the wave trains, we detected P- and S-wave arrivals, from which, given sample dimensions, we derived the corresponding P- and S-wave velocities (v_P, v_S) at each stress regime. To add confidence in S-wave arrival identification, we plotted the wave trains versus stress which allowed us to track the S-wave trajectory with increasing stress (Proestakis *et al*. 2024). This approach aided the wave arrival detection at low stress by referencing the more pronounced arrivals observed at higher stress (Fig. 4).

P-wave (M), shear (G), and bulk (K) moduli were calculated from density and P- or S-wave velocity using Equations 3 to 5 (e.g. Mavko *et al*. 2020):

$$M = \rho v_P^2, \qquad \textit{Eq. 3}$$

$$G = \rho v_S^2, \text{ and} \qquad \textit{Eq. 4}$$

$$K = M - \frac{4}{3}G \qquad \textit{Eq. 5}$$

To quantify porosity changes at different axial stress (σ_{zz}) states, we estimated vertical elastic strain (ε_{zz}), Poisson's ratio (ν) and radial elastic strain (ε_{xx}) at each stress state from elastic moduli using Equations 6 to 8 (Mavko *et al*. 2020):

$$\epsilon_{zz} = \frac{\sigma_{zz}}{M} \qquad \textit{Eq. 6}$$

$$\nu = \frac{M - 2G}{2(M - G)} \qquad \textit{Eq. 7}$$

$$\epsilon_{xx} = \nu \epsilon_{zz} \qquad \textit{Eq. 8}$$

The sample volume in each stress state was estimated using the updated sample length (L) and radius (r):

$$L = (1 + \epsilon_{zz}) L_0 \text{ and} \qquad \textit{Eq. 9}$$

$$r = (1 - \epsilon_{xx}) r_0, \qquad \textit{Eq. 10}$$

where L_0 and r_0 are the sample length and radius in the unload state. Assuming that volume changes reflect closing porosity, we estimated porosity changes from the updated dimensions. Because elastic moduli depend on density (Eqs. 3–5), and density varies with volume, Equations 3–10 must be solved iteratively. In practice, one iteration was sufficient, as changes converged rapidly.

We calculate thermal conductivity as a function

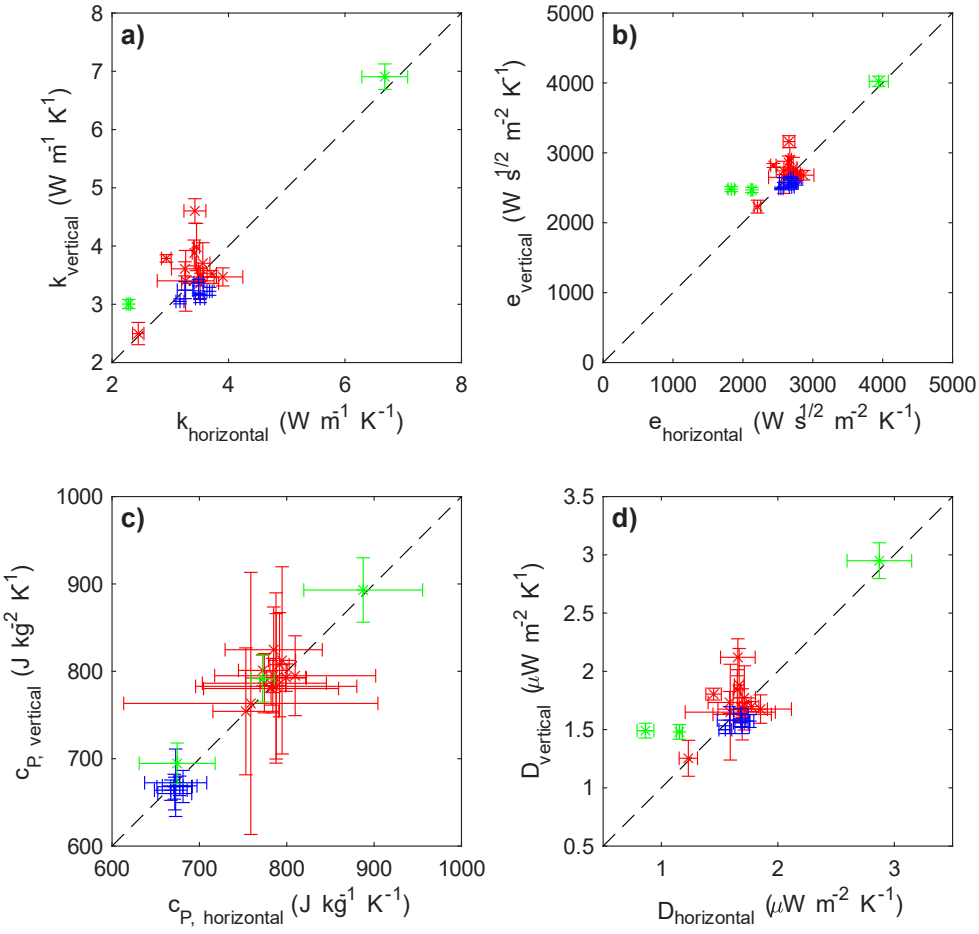


Fig. 8. Horizontal vs. vertical measurements of (a) thermal conductivity, (b) effusivity, (c) specific heat capacity and (d) thermal diffusivity. Dotted lines represent 1:1 realtionship. Error bars are 2 s.d. Legend to colors: see Fig. 6.

of porosity following the model of Orlander *et al.* (2018):

$$\lambda = (1-\alpha)\,\lambda_{lbs} + c_M\,\phi_f + (\alpha - c_M\,\phi)^2 \left(\frac{1 - c_M\,\phi}{\lambda_f} + \frac{V_{sus}}{\lambda_{sus}} + \frac{\alpha - \phi - V_{sus}}{\lambda_{lbs}} \right)^{-1}, \quad \textit{Eq. 11}$$

where subscripts lbs, sus and f refer to load-bearing solids, suspended solids and fluid, respectively. V_{sus} is the volume fraction of suspended solids. The Biot coefficient α is given by (Mavko *et al*. 2020):

$$\alpha = 1 - \frac{K}{K_{min}} \quad \textit{Eq. 12}$$

where K is the dry-state (drained) bulk modulus of the sample (measured) and K_{min} is the bulk modulus of mineral phases. The factor c_M follows the expression of Mortensen *et al*. (1998) for Kozeny's factor:

$$c_M = \left\{ 4\cos\left[\frac{1}{3} \arccos\left(\phi\,\frac{64}{\pi^3} - 1 \right) + \frac{4\pi}{3} \right] + 4 \right\}^{-1} \quad \textit{Eq. 13}$$

For multiphase rocks such as gneiss and amphibolite, thermal conductivities and elastic moduli cannot be calculated without assumptions about textural relations between phases. Heat flow in our samples is approximately parallel to foliation. In this configuration, the Voigt upper bound provides an appropriate description (Beardsmore & Cull 2001; Mavko *et al*. 2020):

$$\lambda_{mix} = \sum_{i=1}^{n_{phases}} f_i \lambda_i \quad and \quad K_{mix} = \sum_{i=1}^{n_{phases}} f_i K_i, \quad \textit{Eq. 14}$$

where f_i is the volume fraction of phase *i*. We use Eq. 14 to compute the suspended and load-bearing solid conductivities (λ_{sus} and λ_{lbs} in Eq. 11) as well as the mineral bulk modulus (K_{min} in Eq. 12).

Temperature profile

Temperatures in the borehole were measured by means of a 4-channel Silixa DTS-M interrogator connected to the two pairs of DTS fibers in the borehole. For temperature calibration of the DTS signal, we used an *in situ* ambient temperature and well-mixed calibration bath containing a 30 m loop of the DTS cable. Measurements were conducted using 0.25 m spatial resolution, with 3 repetitions of 10 min duration for each of the four fibers. Temperatures were derived by applying dual-ended processing using the python module dts-calibration (des Tombe *et al.* 2020; des Tombe *et al.* 2024).

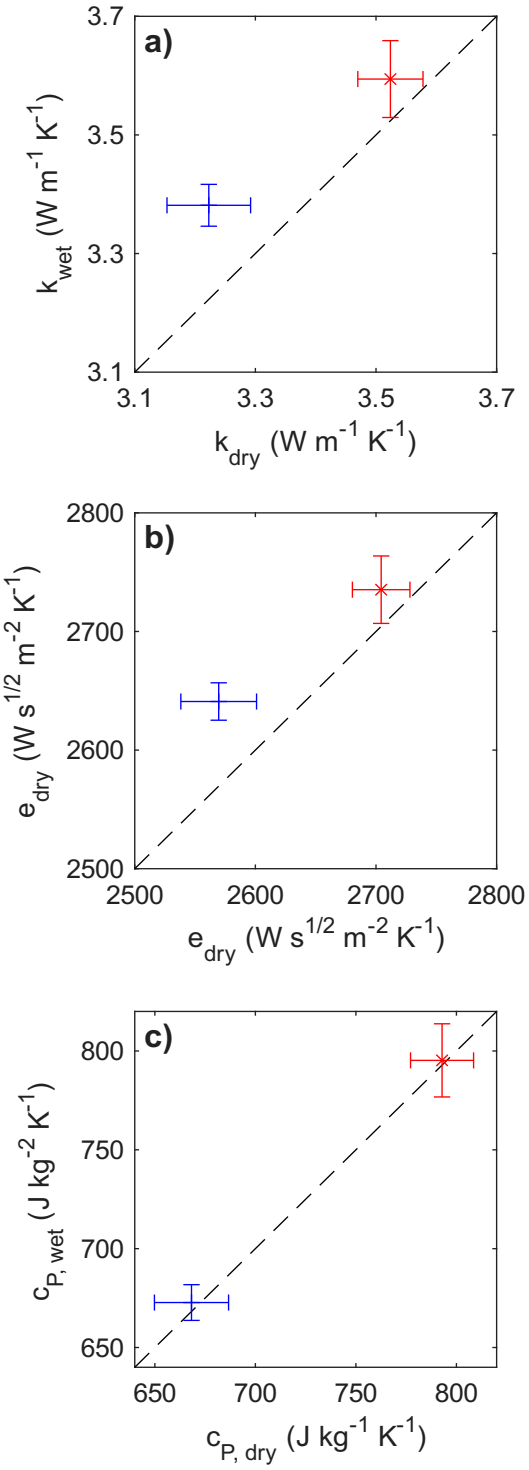


Fig. 9. Comparison of thermal properties in wet and dry states. a) conductivity, b) effusivity and c) specific heat capacity. Note that specific heat capacity was not measured directly but calculated using Eq. 1. Dotted lines represent hypothetical 1:1 line. For legend, see Fig. 6.

Numeric model setup

The aim of the numerical model is to understand how bedrock lithology may influence the thermal regime in permafrost regions, specifically the active layers thickness and timing of annual freeze-thaw cycles.

We modelled transient ground thermal regimes by a one-dimensional finite difference approach using the Matlab toolbox CryoGrid (Westermann *et al.* 2023). The lower boundary condition was a heat flux of 48 mW m^{-2}. To have full parameter control and isolate the effect of lithologies, we used temperature as the upper boundary condition and ignored other contributions to the energy budget. As temperature input, we approximated the 30-year climate normal for Kangerlussuaq (DMI 2024) with harmonic temperature variations (average = –4.6°C, amplitude = 15.5°C, period = 1 year). The model domain was 100 metres of stratigraphy. We used a spin-up of 416 years and evaluated the thermal state in the following (417th) year. This spin-up time was chosen because initial runs suggested that 400 years may be required to obtain steady-state conditions at 100 m depth. Models were set-up as a two-layer stratigraphy with an upper sediment layer (0–6 m thick) overlying bedrock. For bedrock, we used average properties of amphibolite, mafic and felsic gneiss, and a quartz-rich pegmatite. Rock and sediment properties are summarized in Table 2. Grid spacings were 1 cm at 0–6 m depth, 10 cm at 6–15 m, 50 cm at 15–30 m, and 500 cm at 30–100 m.

Results

Petrography

In the GIOS2023-01 core, the gneiss is granitic with varying contents of biotite, titanite, magnetite (Fig. 5g, 6c), muscovite, and garnet (Fig. 5c). In hand specimen, foliation can be recognized in relatively mafic variants and is defined by parallel alignment of mica. Foliation dips 30–70° with no clear trend through the core. Relatively felsic variants tend to be granular and dominated by feldspars and quartz. The point counted sample (GIOS2023-01-239.44) is syenogranitic and have relatively low contents of mafic minerals (Table 3). Alkali feldspar shows varying degrees of perthitic exsolution (Fig. 5h). Relatively homogenous alkali feldspar grains show tartan twinning (Fig. 5f).

The amphibolite is invariantly foliated and dominated by amphibole and plagioclase (Fig. 5b). Minor minerals are quartz, garnet, magnetite, titanite, clinopyroxene and sulfide (Fig. 5b–c). Garnet is typically embedded in silicate minerals. Sulfide minerals are dominated by sub-millimetre pyrite grains (Fig. 6a–b), which are spatially associated with smaller (tenths of micrometres) grains of other sulfide phases, possibly chalcopyrite and troilite (Fig. 6b).

One supracrustal rock (sample GIOS2023-01-137.46) is strongly foliated with abundant biotite with numerous zircon inclusions (Fig. 5a). Other minerals are quartz, feldspars and an opaque mineral. Pegmatite samples are coarse-grained and are dominated by quartz ± feldspar.

Thermal properties

In the vertical direction, the thermal conductivity of

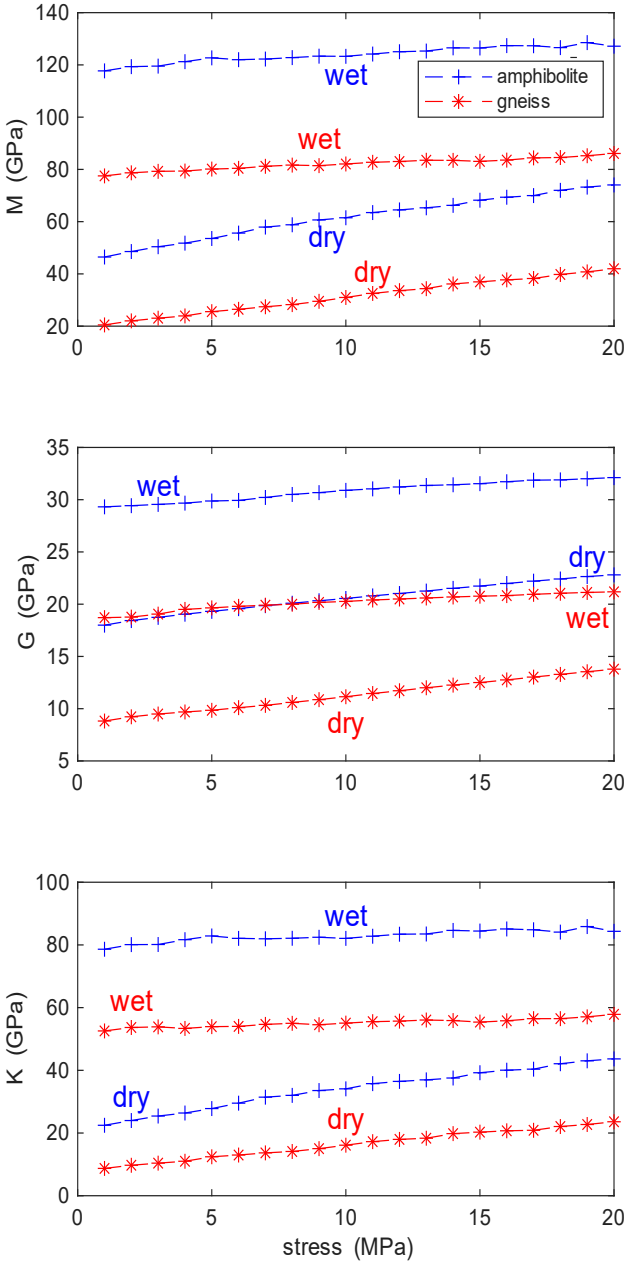


Fig. 10. Elastic moduli variations with stress for samples GIOS2023-01-169.48 (amphibolite) and GIOS2023-01-239.44 (gneiss).

Table 2. Input parameters to the thermal model

	Porosity	Density (kg m^{-3}) of mineral fraction	Volumetric heat capacity (J m^{-3} K^{-1})	Thermal conductivity (W m^{-1} K^{-1})
Sediment	0.5	2651	2081035	3.6
Amphibolite	0.004	3069	2047023	3.2
Mafic gneiss	0.004	2651	2081035	3.6
Felsic gneiss	0.004	2621	2107284	3.9
Pegmatite	0.004	2622	2342038	6.9

Gneiss and amphibolite properties from this study, sediment porosity from Zastruzny *et al*. (2024).

amphibolite is relatively low (3.1 ± 0.4 to 3.4 ± 0.6 W m^{-1} K^{-1}, 2 s.d.) compared with most gneiss samples (Fig. 7a). Although one sample (GIOS2023-01-130.47) yielded a vertical conductivity as low as 2.5 ± 0.2 W m^{-1} K^{-1} (2 s.d.), most gneiss samples have higher conductivity, ranging up to 4.6 ± 0.2 W m^{-1} K^{-1} (2 s.d.; Fig. 7a). With its relatively high density and low specific heat capacity, the amphibolite (ϱ = 3049 ± 2 to 3088 ± 2 kg m^{-3}, c_P = 660 ± 19 to 672 ± 39 J kg^{-1} K^{-1}, 2 s.d.) it is clearly different from the host-rock gneiss (ϱ = 2603 ± 1 to 2703 ± 1 kg m^{-3}, c_P = 754 ± 73 to 825 ± 49 J kg^{-1} K^{-1}, 2 s.d.; Fig. 7b–c).

We calculate anisotropy as the ratio between thermal conductivities measured on the horizontal and vertical sample surface ($k_{horizontal}/k_{vertical}$). Although our measurements technique only interacts with a millimetre-scale sample volume and, thus, are not one-dimensional on the macroscopic scale, we are able to resolve some anisotropy, possibly related to mineral orientations and preferred orientations of microcracks. Calculated in this way, the amphibolite shows higher conductivity in the horizontal direction but limited anisotropy overall (1.00 ± 0.06 to 1.14 ± 0.07, 2 s.d.). In contrast, the anisotropy of the gneiss is more variable (1.00 ± 0.03 to 1.3 ± 0.1, 2 s.d.) and it varies whether the vertical or horizontal is more conducting, possibly because of variations in foliation orientation. One quartz-rich pegmatite sample (GIOS2023-01-109.06) has a relatively high thermal conductivity of 6.9 W m^{-1} K^{-1} (Fig. 7a) and the supracrustal rock (sample GIOS2023–01-137.46) has a very high anisotropy of 1.8 (Fig. 8a). The measured thermal diffusivities in samples from the amphibolite (1.50 ± 0.03 to 1.65 ± 0.04 µW m^2 K^{-1}, 2 s.d.) overlap with the lowest values measured for gneiss samples, but values for gneiss samples extend as high as 2.1 ± 0.2 µW m^2 K^{-1} (2 s.d.; Fig. 7d, 8d).

Specific heat capacity calculated from vertical and horizontal measurements were always identical within the uncertainty (Fig. 8c). Since specific heat capacity is a scalar property, this observation is expected if effusivity and conductivity are measured accurately.

Wet samples yielded slightly higher effusivities (3% in amphibolite, 1 % in gneiss) and thermal conductivities (5% in amphibolite, 3 % in gneiss) compared dry state, whereas the calculated specific heat capacities were identical within the associated uncertainties (Fig. 9a–c).

Elastic properties

Elastic moduli variations with stress are summarized in Fig. 10. Shear (Fig. 10b) and bulk (Fig. 10c) moduli are higher in amphibolite (G = 18–23 GPa; K = 23–44 GPa in dry sample) than in gneiss (G = 9–14 GPa; K

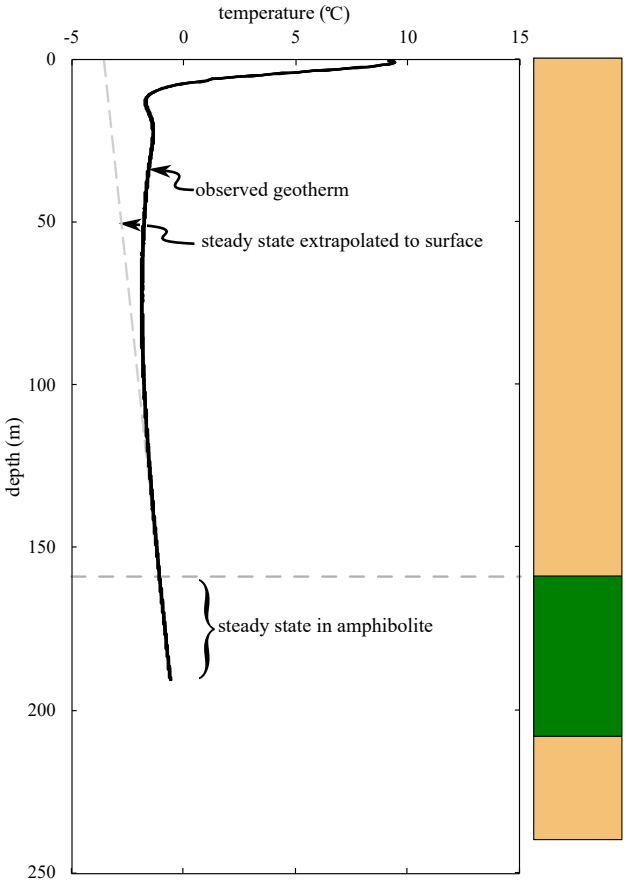


Fig. 11. Observed geotherm on 20 August, 2024. Superimposed on the geotherm is a linear extrapolation of the steady state interval (158.76 and 190.7 m b.g.s.) to the surface. A simplified lithological log to the right shows the distribution of gneiss and amphibolite.

Table 3. Modal composition of selected samples and physical properties of the rock-forming minerals and pore fluids

	alkali feldspar	plagioclase	quartz	amphibole	clinopyroxene	titanite	biotite	muscovite	magnetite	sulfides[a]	air	water	ice
Modal prop. (%) in sample -169.48 (amphibolite)	–	17 ± 8	6 ± 8	74 ± 4	0.2 ± 8.7	2 ± 9	–	–	–	0.2 ± 8.7	–	–	–
Modal prop. (%) in sample -239.44 (gneiss)	40 ± 5	20 ± 6	37 ± 5	–	–	0.3 ± 6.2	3 ± 6	0.3 ± 6.2	0.7 ± 6.2	–	–	–	–
k (W m^{-3} K^{-1})	1.7[b]	2.0[b]	7.7[b]	3.1[b]	3.8[b]	–	2.3[b]	2.5[b]	5.1[b]	19.2[b]	0.0[e]	0.6[e]	2.2[d]
ρ (kg m^{-3})	2573[b]	2642[b]	2647[b]	3111[b]	3275[b]	3500[c]	2886[b]	2834[b]	5145[b]	4915[b]	–	–	–
c_p (J kg^{-1}K^{-1})	735[f]	760[f]	739[f]	705[c]	811[f]	810[c]	1375[g]	1408[f]	619[f]	62[f]	–	–	–
K (GPa)	46.7[i]	64.2[i]	37.0[i]	93.0[i]	94.1[i]	–	59.7[i]	5.8[i]	161.4[i]	147.4[i]	0	2,3	9,1
G (GPa)	23.6[i]	25.6[i]	44.0[i]	57.0[i]	57.0[i]	–	42.3[i]	3.3[i]	91.4[i]	132.5[i]	0	0	3.5[i]

Modal proportions and uncertainties are calculated following Galehouse (1971), uncertainties are 2 s.d.
[a]Sulfides are mainly pyrite and physical constants are listed for pyrite. [b]Horai (1971). [c]Waples & Waples (2004). [d]Huang *et al.* (2013). [e]Sears *et al.* (1987). [f]Anderson (2017). [g]White (2013). [h]Clauser & Huenges (1995). [i]Mavko *et al.* (2020). [j]Angel *et al.* (1999). [k]Salje *et al.* (2011). [l]Brown & Abramson (2016).

= 9–24 GPa), and higher in water-saturated than in dry state (i.e., G = 29–32 GPa; K = 77–84 GPa in wet amphibolite and 19–21 GPa; K = 53–58 GPa in wet gneiss). In all samples, shear and bulk moduli increase with axial stress in the interval 0–20 MPa in a relationship that appear linear.

Temperature profile and geothermal gradient

The temperature profile from August 20th, 2024, has maximum value at the surface (9.3°C). With depth, temperatures decrease to a local minimum (–1.7°C) at 12.6 m b.g.s., increase to local maximum (–1.3°C) at 23 m b.g.s., decrease to global minimum (–1.8°C) at 73 m b.g.s., and finally increase to –0.6°C at 190 m b.g.s. (Fig. 11). Thus, permafrost thickness is >190 m. In comparison, van Tatenhove & Olesen (1994) estimated the permafrost thickness to be 127 ± 31 m at 50 m above sea level. The temperature measurements suggest a constant geothermal gradient in the interval 158.76–190.65 m b.g.s. (amphibolite). For each of the four temperature profiles, we calculate the geothermal gradient in this interval as a weighted least squares regression (Taylor 1997). Results range from 0.0149 ± 0.0002 to 0.0160 ± 0.0003 °C/m. A linear projection of these gradients to the surface suggests surface temperatures of –3.67 ± 0.05 to –3.42 ± 0.04°C (Fig. 11).

Discussion

Mineralogy and pore fluid as controlling parameters for physical properties of the studied samples

In rocks, heat is conducted through the constituent minerals and pore fluid. Although porosity estimates for the gneiss and amphibolite are low, the influence of (low-conductivity) pore fluid is evidenced by their relatively low conductivities relative to that of their mineral constituents. In the natural settings we aim to understand, pore fluid may be water, ice, or some mix, with very different thermal properties. In addition, the porosity may vary with increasing lithostatic pressure, influencing the thermal conductivity. Thus, we begin the discussion by evaluating the influence of pore fluid and lithostatic pressure on the thermal conductivity.

Porosity variations with depth

The porosity estimates for gneiss and amphibolite are 0.45 ± 0.36 % and 0.4 ± 0.2 %, respectively. The reported uncertainties are propagated from the varia-

tion in readings in the scales and are believed to reflect water on the sample surface which evaporates over time. Uncertainties on the scales and caliper are negligible in comparison.

The vertical elastic strain, derived from the measured modulus at each stress level (Eq. 6), is minimal, indicating that the associated reduction in porosity is minor. Specifically, the initial porosity of sample 169.48 was 0.4 % and decreased to 0.38 % under an applied axial stress of 20 MPa, and sample 239.44 even less. Thus, porosity reductions are within the uncertainty of the no-stress porosity estimates. This minor porosity reduction can be attributed to the closure of pre-existing microfractures, which improved the grain-to-grain contact and contributed to the observed increase in the measured elastic modulus (Fig. 10).

Thermal conductivities with different pore fluids

Although thermal conductivity of ice, water and air span two orders of magnitude (Table 3), we see limited difference between wet and dry measurements (Fig. 9). This is a consequence of the low porosity in the rocks. Thus, regardless of the applied mixing model, the thermal conductivity is dominated by mineral properties. For instance, changing pore fluid from ice to air will change the upper Voigt bound (Eq. 14) in the gneiss by as little as 0.01.

Variation in thermal conductivities with stress and depth

In this section, we discuss the relevant thermal conductivity of minerals and predict the variations in thermal conductivity with increasing stress. As stress is directly related to depth, this allow us to discuss the possibility of changing conductivity with depth.

Thermal conductivities as functions of stress – In Fig. 12, we predict the variations in thermal conductivity with increasing stress (Eqs 11–13). Given that all studied rocks are steeply foliated, we estimate mineral conductivities as the Voigt upper bound (Eq. 14). Uncertainty intervals (grey shading) are calculated from uncertainty in initial porosity and are expectedly broad because of the large uncertainty in this parameter. For the gneiss, the discrepancy between measured conductivity (at 0 MPa) and the predicted conductivity at low stress (0.1 MPa) is fully explained by the uncertainty stemming from porosity (Fig. 12a). In the amphibolite, the predicted value appears slightly low (Fig. 12b). In this sample, uncertainty arises from the relatively large uncertainty on the volume proportion of highly conducting pyrite stemming from low volume proportions and, thus, poor counting statistics from point counting (Table 3).

We conduct a simple sensitivity analysis by changing the proportion of pyrite (from 0.002 to 0.08), quartz (from 0.056 to 0.057) and amphibole (from 0.8 to 0.7) and normalizing remaining minerals to a sum of 1. Although semi-arbitrarily chosen, the adjusted mineral proportions are all within the 2 s.d. uncertainty interval obtained from point counting. With the adjusted mineral proportions, we predict a density of 3091 kg m^{-3} as obtained from measurement. The adjusted mineral proportions also predict conductivities in good agreement with measurements and are preferred in the following discussion ('adjusted' in Fig. 12b).

Thermal conductivity changes with depth – In section 'Crustal heat flux at the study site', we calculate the local heat flux from the geothermal gradient at 158.76–207.81 m, corresponding to a lithostatic pressure of 4.3–4.9 MPa. Between 1 and 5 MPa, amphibo-

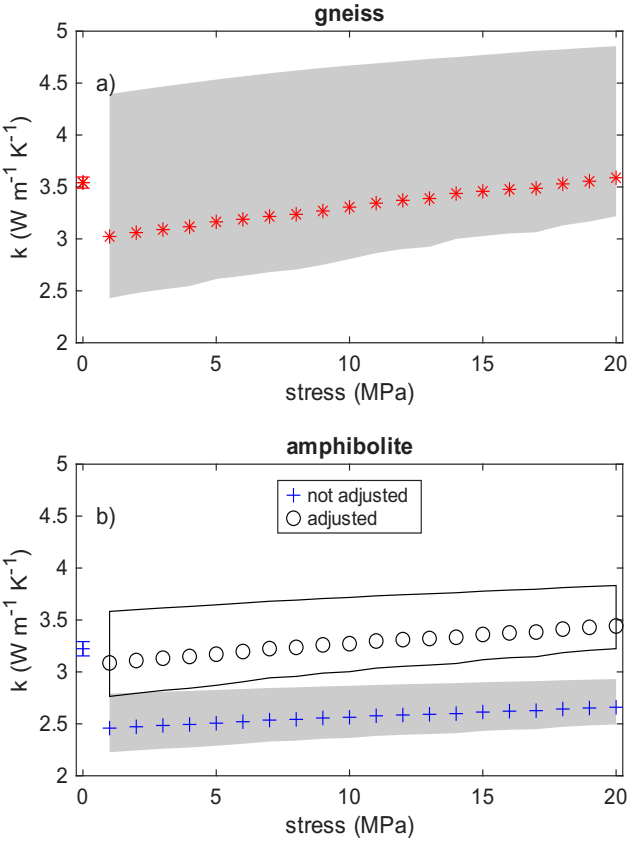


Fig. 12. Predicted thermal conductivities of gneiss (a) and amphibolite (b). Data points at 0 MPa are measured values (samples GIOS2023-01-169.48 and -239.44). Grey shading represent credible intervals obtained from uncertainty in porosity measurement. Other uncertainties, e.g. in mineral proportions, have not been propagated. In (b), adjusted values were calculated from a slight adjustment to the modal proportion (see text).

lite conductivities are expected to increase by 0.09 W m^{-1} K^{-1} (Fig. 12b). As this is less than the uncertainties, we do not adjust thermal conductivity in that section with depth. Similarly, we model the upper 100 m in Section 'Modeling the transient thermal regime in and above different bedrock lithologies', corresponding to a lithostatic pressure of 2.4 MPa, suggesting a conductivity increase in the order of 0.06 W m^{-1} K^{-1} in gneiss. As this is an order of magnitude lower than the measurement uncertainty, we do not adjust for conductivity changes in the numerical model.

Crustal heat flux at the study site

In the amphibolite (158.76–207.81 m b.g.s.), a constant geothermal gradient between 158.76 and 190.65 m b.g.s. (Fig. 11) indicates steady state heat flow. A linear projection of the geothermal gradient from this interval to the surface indicates average surface temperatures of –3.67 ± 0.05 to –3.42 ± 0.04°C, i.e. 0.8 to 1.1°C warmer than the 1991–2020 climate normal from the Kangerlussuaq settlement (–4.5°C, DMI 2024). The settlement is topographically c. 200 m lower than the borehole location. As air temperature decreases with elevation, the relatively higher surface temperature in our projection suggests paleoclimatic rather than topographic effects. Climate reconstructions of the Kangerlussuaq area suggest that 1.5–2.0°C warmer climate has occurred at times within the last 2000 years (Strunk *et al.* 2024), possibly explaining why the projection is warmer than the present-day temperatures. Another possible explanation relates to the recent denudation of a sediment layer from the borehole location, which may have warped the geothermal gradient to 158.76 m b.g.s. and shifted the steady-state temperature profile between 158.76–207.81 m b.g.s. upwards without changing the gradient. In principle, heat flux may also be influenced by thermal transport by fluid movements in joints. However, the density of joints is typically very low (0 to <10 per 2.5 m), although two intervals at 105 and 120 m b.g.s. are higher at 20 and 50 per 2.5 m, respectively. Moreover, the entire steady state interval is below 0°C and known to freeze during drilling, suggesting limited fluid flow. The transient nature of the upper part of the temperature profile has no implications for the further analysis in this paper and will not be discussed in more detail.

Applying an average thermal conductivity of 3.2 ± 0.2 W m^{-1} K^{-1} for the amphibolite along with the observed temperature gradient, we calculate a heat flux of 48 ± 4 to 51 ± 4 mW m^{-2}. Although our reported heat flux values have not undergone a paleoclimatic correction, we believe that the linear geothermal gradient in the amphibolite provides strong evidence for steady-state heat conduction that is not influenced by the thermal perturbations observed above 158.76 m b.g.s. Predictions of the local heat flow from regional heat flow maps vary between c. 30 and 60 mW m^{-2} (Rezvanbehbahani *et al.* 2017; Artemieva 2019; Martos *et al.* 2018; Greve 2019; Colgan *et al.* 2022; Freienstein *et al.* 2024). A discussion of different methodological approaches to regional heat flux estimation is beyond the scope of this paper. Instead, we observe that our measured heat flux is bounded by higher as well as lower literature values. Given the linear shape of the geothermal gradient, the surface projection being consistent with slightly warmer Holocene surface temperatures, and the fact that the calculated thermal heat flux is consistent with previously published heat flux estimates, we consider our values a robust measurement of the regional heat flux. For the finite element modeling, we use the heat flux calculated in this section.

Modeling the transient thermal regime in and above different bedrock lithologies

The aim of the numeric modeling is to investigate

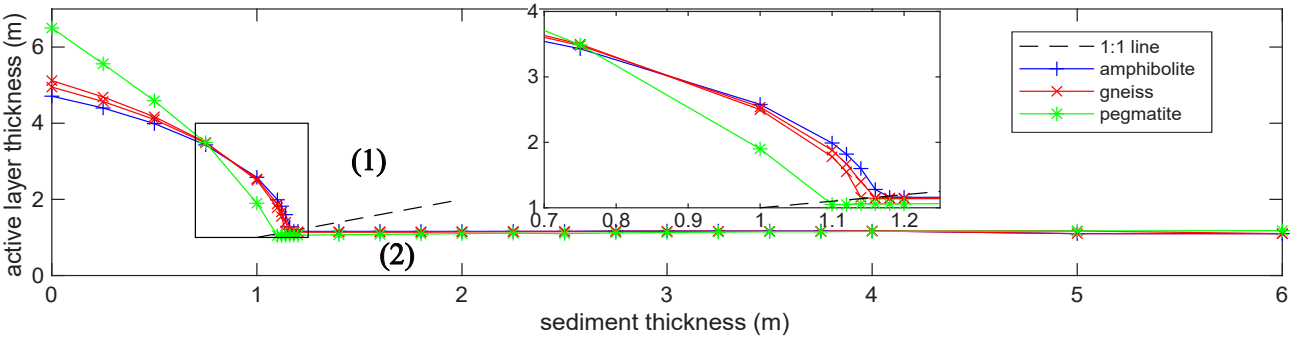


Fig. 13. Modelled active layer thicknesses as a function of sediment thickness for three lithologies (amphibolite, gneiss, and pegmatite). The two red curves represent mafic and felsic gneiss, respectively, and thus bracket the realistic interval for gneiss properties in the core. The dotted line separates situation 1 (active layer thickness > sediment thickness) from situation 2 (active layer thickness < sediment thickness). The insert highlights the interval where curves cross.

how the thermal regime is locally influenced by bedrock lithology. We present modeling results for gneiss and amphibolite (which we know is extensive), and for pegmatite. The dimensions of the pegmatite are not known in detail and may be too small to be realistically modelled in a one-dimensional model. However, the pegmatite can be considered an extreme contrast to relatively dense amphibolite with low thermal conductivity.

Active layer thicknesses

In the numeric models, we investigate how the ground thermal regime is influenced by relevant bedrock properties. The results of the models fall in two groups: (1) When the sediment thickness is relatively low, it is exceeded by the active layer thickness, and the base of the active layer is in the bedrock. (2) The sediment is relatively thick, and the base of the active layer is located in the sediment above the bedrock. In Fig. 13, these situations are separated by a dotted line.

With no sediment overlying bedrock, latent heat of freezing and thawing is minimal because of the low porosity in the bedrock, and the thermal regime is mainly controlled by the bedrock properties. The amphibolite's relatively high density, specific heat capacity and low thermal conductivity, reduce the penetration of seasonal temperature variations in the amphibolite, compared to the gneiss and pegmatite.

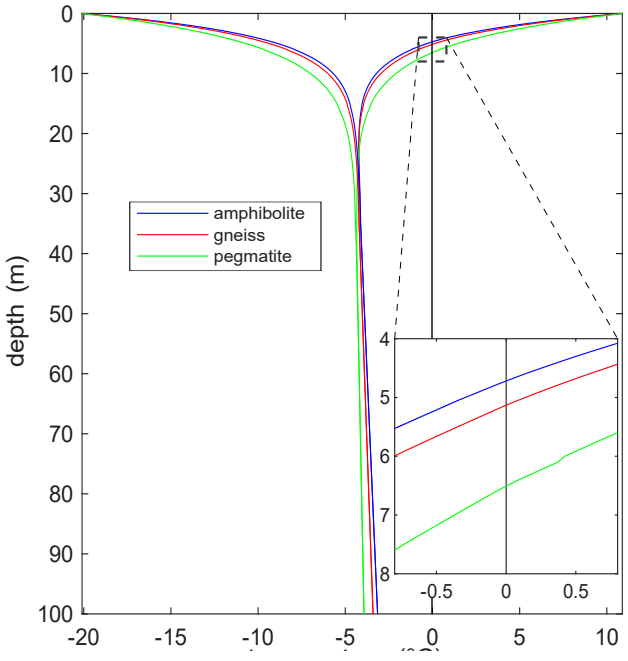


Fig. 14. Minimum and maximum temperature during one model year for the three lithologies (amphibolite, felsic gneiss, and pegmatite) in the full model domain. No sediment in models.

Thus, the amphibolite is relatively inert to temperature changes and yields low active layer thickness (4.71 m) compared to the gneiss (4.95–5.12 m) and pegmatite (6.50 m; Fig. 14). As the sediment thickness increases, the modelled active layer thicknesses decrease and converge (Fig. 13). At >0.75 m sediment, the active layer of temperature-inert amphibolite is thinner than that in gneiss and pegmatite.

This inversion of the curves at ~0.75 m sediment reflects how heat is distributed in the models. At low sediment thickness, most of the temperature fluctuation takes place in the bedrock. In these model runs, thermally inert amphibolite yields relatively low active layer thickness. With higher sediment thickness, more heat diffuses through the sediment than through the bedrock. When this is the case, the thermally inert amphibolite acts as a heat sink because it remains relatively cold during spring heating and warm during autumn cooling. This creates high geothermal gradients close to the sediment-amphibolite interface relative to sediment-gneiss and sediment-pegmatite interfaces (Fig. 15), enhancing fast diffusion of heat and causing relatively thin active layers.

In situation (2) (active layer thickness > sediment thickness), modelled active layer thicknesses vary between 1.05 and 1.18 m. Between ~1.1 and ~4 m sediment thicknesses, the active layer thickness above amphibolite exceeds that above pegmatite with

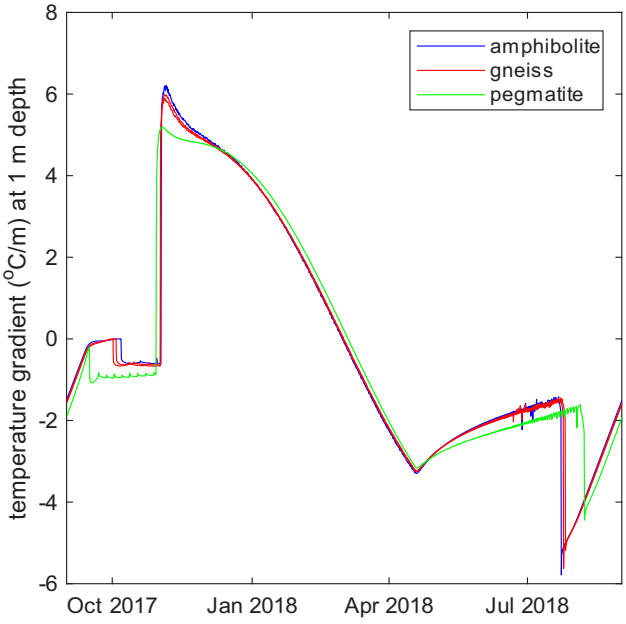


Fig. 15. Temperature gradients at the bedrock-sediment interface (sediment thickness = 1 m) for one modelled year. The absolute values of heat flux peak during autumn cooling and spring heating with some delay, i.e. November (autumn cooling signal) and July-August (spring heating signal). In all cases, the absolute value at the interface between sediment and thermally inert amphibolite exceeds that of sediment-gneiss and sediment-pegmatite interfaces.

gneiss being intermediate (Fig. 13). At >4 m sediment thickness, active layer thicknesses converge and the influence of underlying bedrock decreases.

Timing of freezing and thawing

The timing of freezing and thawing is investigated in time-depth space in Fig. 16. At the surface, all lithologies freeze and thaw at the same time. With increasing depth, the isotherms differ with pegmatite being earliest to freeze and thaw, and amphibolite latest. At 1 m depth, the difference in thawing is in the order of days, growing to tens of days at 2–3 m and >1 month at >4 m depth. For sediment overlying bedrock (not shown), the difference between gneiss and amphibolite is not resolvable with the models' 6-hour time-steps, and the difference between pegmatite and gneiss/amphibolite reduce to 6–12 hours.

Implications for human societies

Seasonal or climatic changes to the ground thermal regime cause several risks to infrastructure and humans, including changes to bearing capacity, frost heaving, active layer detachment and debris flows (McRoberts & Morgenstern 1974; Zimmerman & Haeberli 1992; Andersland & Ladanyi 1994; Leibman 1995; Lewkowicz 2007; Lewkowicz & Hartshorn 1998; Sattler *et al.* 2011; Agergaard & Ingeman-Nielsen 2012; Hjort *et al.* 2022). Changes to bearing capacity and frost heaving primarily affect sediments. Thus, in settings where the active layer extends into the underlying bedrock (situation 1, Fig. 13), lithological differences have negligible impact on these hazards. Where sediment is thicker than the active layer (situation 2), the difference in heaving is also expected to be minor as the differences in active-layer thickness are typically in the order of centimetres.

Active layer detachments and debris flows occur when the active layer melts, creating high porewater pressure. This reduces the effective shear strength between frozen and unfrozen ground, creating downslope movement at the interface between frozen and unfrozen ground. In situation (1), our modeling suggests that the timing of thawing depends on the bedrock properties. For any given time during spring thawing, the sediment above gneiss or pegmatite will have melted to a greater depth than sediment over amphibolite. If all other factors (e.g., precipitation, and sediment properties and thickness) remain constant, our modeling suggests that the thawed layer will be thickest above pegmatite and thinnest above amphibolite. This situation can lead to positive feedback loops accelerating the permafrost degradation in sediment overlying gneiss before that overlying amphibolite (Devoie *et al.* 2019; Chen *et al.* 2023; Wang *et al.* 2025; Luo *et al.* 2025), further driving the difference between the lithologies. Similarly, rock slopes of gneiss may be more susceptible to failure than those of amphibolite because rock slope failures are directly related to melting of pore ice (Gruber & Haeberli 2007; Vivani *et al.* 2020; Marcer *et al.* 2024) and our modeling suggests that the active layer thickness (Fig. 14) and timing of thawing (Fig. 16) is directly related to rock properties.

Conclusions

We present new data on physical properties (elastic moduli in the interval 0–20 MPa, thermal conductivity and effusivity, density and specific heat capacity in unloaded state), mineralogy, and porosity for

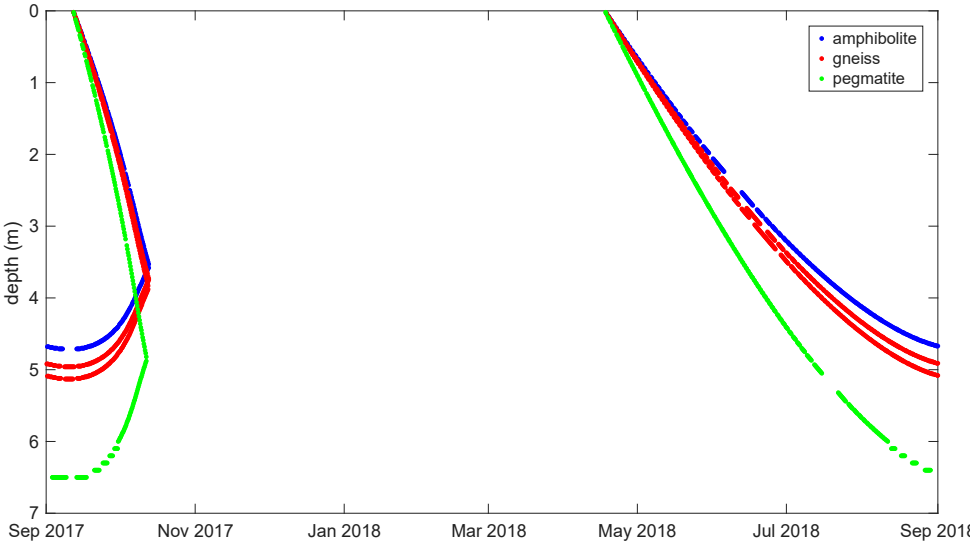


Fig. 16. Timing of freezing (September–October) and thawing (May–September) for amphibolite, mafic and felsic gneiss, and pegmatite in the last modelled year. Model runs with no sediment cover.

rocks from the GIOS2023-01 drill core (Kangerlussuaq, West Greenland) and temperature data from the corresponding borehole. The rocks are mainly amphibolite and gneiss, and represent a metamorphosed Kangâmiut dyke intersecting older gneiss. This structure is common in large parts of West Greenland.

Integration of the datasets show that gneiss and amphibolite have low porosity, around 0.4 %. In the stress interval 0–20 MPa (corresponding to a depth interval of 0–760 metres), elastic moduli change significantly, while change in porosity is negligible, indicating the closure of pre-existing microfractures and improvement of grain-to-grain contact. Thermal conductivity was measured only in unloaded state, but theoretical considerations suggest that it varies insignificantly in the stress interval studied.

Using our measured rock properties, we modeled active layer thickness for scenarios with and without sediment cover. Bedrock lithology alone produces active layer thickness of 4.7 m in amphibolite and 6.5 m in pegmatite. Where sediment overlies bedrock, the model shows that bedrock properties influence active layer thickness for sediment covers up to 4 m thick. At sediment thickness >4 m, bedrock influence diminishes and active layer thickness converges to ~1.1 m. This degree of bedrock control on sediment thermal regime is interesting and should be tested in future field studies and predictive models for permafrost-related surface phenomena.

Acknowledgments

We thank K. Tveit, S.-J. J. Berthelsen, M.G.S.C. Heretis, I.P.A. Josvassen, A.L.S.H. Kielsen, E.R. Kjældgaard, H. Magnusson, T.R. Poulsen, I. Paulsen, M.C.S. Hansen, C.P. Hansen, and A.B. Abrahamsen for their hard work during drilling and, as for the latter, during core logging and sampling. P.K. Jensen's thorough feedback, Y. Maystrenko constructive review and O. Bennike's skillful editorial handling of the manuscript is highly appreciated. This research was generously funded by Ingeniør Kaptajn Aage Nielsens Familiefond. It was also supported by the EU Horizon Europe programme, grant agreement No. 101133587 (ILLUQ). The borehole was established as part of the Greenland Integrated Observing System (GIOS) funded by the Danish National Fund for Research Infrastructure (NUFI) under the Ministry for Higher Education and Science.

Data availability

All data presented in this publication are available at https://doi.org/10.11583/DTU.32848589.
Supplementary A: The file contains parameters relevant for transient thermal model: Thermal conductivity (vertical and horizontal measurements), density, effusivity (vertical and horizontal measurements), and specific heat capacity (Eq. 1).
Supplementary B: The file contains borehole measurement raw data. Three repetitions of four measurements.
Supplementary C: The file contains elastic parameters of gneiss and amphibolite in dry and wet state.

References

Agergaard, F.A. & Ingeman-Nielsen, T. 2012: Development of bearing capacity of fine grained permafrost deposits in western Greenland urban areas subject to soil temperature changes. In: Brian, M. & Guy, D. (eds): Cold regions engineering 2012: Sustainable infrastructure development in a changing cold environment, 82–92. American Society of Civil Engineers. https://doi.org/10.1061/9780784412473.009

Andersland, O.B. & Ladanyi, B, 1994: An introduction to frozen ground engineering, 352 pp. Dordrecht: Springer Science+Business Media.

Anderson, R.S. 1998: Near-surface thermal profiles in alpine bedrock: Implications for the frost weathering of rock. Arctic and Alpine Research 30, 362–372. https://doi.org/10.1080/00040851.1998.12002911

Anderson, G. 2017: Thermodynamics of natural systems – theory and applications in geochemistry and environmental science, 413 pp. New York: Cambridge University Press.

Angel, R. J., Kunz, M., Miletich, R., Woodland, A.B., Koch, M. & Knoche, R.L. 1999: Effect of isovalent Si,Ti substitution on the bulk moduli of Ca(Ti1-xSix)SiO5 titanites. American Mineralogist 84, 282–287

Artemieva, I.M., 2019: Lithosphere thermal thickness and geothermal heat flux in Greenland from a new thermal isostasy method. Earth-Science Reviews 188, 469–481. https://doi.org/10.1016/j.earscirev.2018.10.015.

Beardsmore, G.R. & Cull, J.P. 2001: Crustal heat flow: A guide to measurement and modelling, 324 pp. Cambridge: Cambridge University Press.

Brown, J. M. & Abramson, E.H. 2016: Elasticity of calcium and calcium-sodium amphiboles, Physics of the Earth and Planetary Interiors 261, Part B, 161–171, https://doi.org/10.1016/j.pepi.2016.10.010.

Carlson, A.E., Reyes, A.V., Sillett, K., Wilcken, K.M. & Rood, D.H. 2021: Southwest Greenland ice-sheet retreat during the 8.2 ka cold event. Quaternary Science Reviews 268, 107101, https://doi.org/10.1016/j.quascirev.2021.107101.

Chen, L., Fortier, D., McKenzie, J.M., Voss, C.I. & Lamontagne-Hallé, P. 2023: Subsurface porewater flow accelerates talik development under the Alaska highway, Yukon: a prelude to road collapse and final permafrost thaw? Water Resources Research 59, e2022WR032578. https://doi.org/10.1029/2022WR032578

Clauser, C. & Huenges, E. 1995: Thermal conductivity of rocks and minerals. In Ahrens, T.J. (ed.): Rock physics & phase relations. https://doi.org/10.1029/RF003p0105

Colgan, W. *et al.* 2022: Greenland geothermal heat flow data-

base and map (version 1). Earth Systems Science Data 14, 2209–2238. https://doi.org/10.5194/essd-14-2209–2022

C-Therm Technologies Ltd. 2013: TCi operator manual, Rev. O. Fredericton, NB: C-Therm Technologies Ltd. TCi Operator Manual, Rev. O.

des Tombe, B., Schilperoort, B. & Bakker, M. 2020 : Estimation of temperature and associated uncertainty from fiber-optic Raman-spectrum distributed temperature sensing. Sensors 20, 2235. https://doi.org/10.3390/s20082235

des Tombe, B. F. & Schilperoort, B. 2024: Dtscalibration Python package for calibrating distributed temperature sensing measurements (v3.1.0). Zenodo. https://doi.org/10.5281/zenodo.13759548

Devoie, É.G., Craig, J.R., Connon, R.F. & Quinton, W.L. 2019 : Taliks: a tipping point in discontinuous permafrost degradation in peatlands. Water Resources Research 55, 9838–9857. https://doi.org/10.1029/2018WR024488

DMI (Danish Meteorological Institute), 2024: DMI Vejrarkiv. https://www.dmi.dk/vejrarkiv/normaler-gronland/ (accessed 17 December, 2024).

Freienstein, J., Szwillus, W., Wansing, A. & Ebbing, J. 2024: Statistical appraisal of geothermal heat flow observations in the Arctic. Solid Earth 15, 513–533. https://doi.org/10.5194/se-15-513–2024

Galehouse, J.S. 1971: Point counting. In: Carver, R.E. (ed.): Procedures in sedimentary petrology, 329 pp. New York: John Wiley and Sons.

Greve, R. 2019: Geothermal heat flux distribution for the Greenland ice sheet, derived by combining a global representation and information from deep ice cores. Polar Data Journal 3, 22–36. https://doi.org/10.20575/00000006, 2019.

Gruber, S. & Haeberli, W. 2007: Permafrost in steep bedrock slopes and its temperature-related destabilization following climate change. Journal of Geophysical Research 112, F02S18. https://doi.org/10.1029/2006JF000547

Harris, S.A., Brouchkov, A. & Guodong, C. 2018: Geochryology: Characteristics and use of frozen ground and permafrost landforms, 765 pp. Leiden: CRC Press/Balkema.

Hjort, J., Streletskiy, D., Doré, G., Wu, Q., Bjella, K. & Luoto, M. 2022: Impacts of permafrost degradation on infrastructure. Nature Reviews Earth and Environment 3, 24–38. https://doi.org/10.1038/s43017-021-00247-8

Horai, K.-I. 1971: Thermal conductivity of rock-forming minerals. Journal of Geophysical Research 76, 1278–1308.

Hrbáček, F., Kňažková, M., Láska, K. & Pastíriková, L. 2025: Active layer warming and thickening on CALM-S JGM, James Ross Island, in the Period 2013/14–2022/23. Permafrost and Periglacial Processes 36, 378–389. https://doi.org/10.1002/ppp.2274.

Huang, W., Li, Z, Liu, X., Zhao, H., Guo, S. & Jia, Q 2013: Effective thermal conductivity of reservoir freshwater ice with attention to high temperature. Annals of Glaciology 54, 189–195. https://doi.org/10.3189/2013AoG62A075

Ingeman-Nielsen, T. 2026: Kangerlussuaq Airport: Permafrost and geotechnical conditions. Kongens Lyngby: DTU Sustain report.

Kokfelt, T.F. *et al*. 2023: Digital 1:500 000 scale geological map of Greenland, version 2.0. Copenhagen: Geological Survey of Denmark and Greenland.

Korstgård, J., Mengel, F., Glassley, W. & Sørensen, K. 2024: The Kangâmiut dykes in West Greenland: markers of the tectono-metamorphic evolution of the southern Nagssugtoqidian orogen and its foreland. GEUS Bulletin 58. https://doi.org/10.34194/geusb.v58.8312

Leibman, M. O. 1995: Cryogenic landslides on the Yamal Peninsula, Russia: preliminary observations. Permafrost and Periglacial Processes 6, 259–264. https://doi.org/10.1002/ppp.3430060307

Lesnek, A.J., Briner, J.P., Young, N.E. & Cuzzone, J.K. 2020: Maximum southwest Greenland ice sheet recession in the early Holocene. Geophysical Research Letters, 47, e2019GL083164. https://doi.org/10.1029/2019GL083164

Levy, L.B., Kelly, M.A., Applegate, P.A., Howley, J.A. & Virginia, R.A. 2018: Middle to late Holocene chronology of the western margin of the Greenland Ice Sheet: A comparison with Holocene temperature and precipitation records. Arctic, Antarctic, and Alpine Research 50, e1414477-1-e1414477-12. https://doi.org/10.1080/15230430.2017.1414477

Lewkowicz, A.G. & Hartshorn, J. 1998: Terrestrial record of rapid mass movements in the Sawtooth Range, Ellesmere Island, Northwest Territories, Canada. Canadian Journal of Earth Sciences 35, 55–64. https://doi.org/10.1139/e97–086

Lewkowicz, A.G. 2007: Dynamics of active-layer detachment failures, Fosheim Peninsula, Ellesmere Island, Nunavut, Canada. Permafrost and Periglacial Processes 18, 89–103.

Lewkowicz, A.G. *et al*. 2025: Glossary of permafrost science and engineering. Canadian Permafrost Association. http://doi.org/10.3138/cpa-gpse

Luo, D., Liu, J., Chen, F. & Li, S. 2025: Observed talik development triggers a tipping point in marginal permafrost of the Qinghai-Xizang Plateau. Geoscience Frontiers 16, 102122.

Marcer, M., Duvillard, P.-A., Tomaškovičová, S., Nielsen, S. R., Revil, A. & Ingeman-Nielsen, T. 2024: Modelling present and future rock wall permafrost distribution in the Sisimiut mountain area, West Greenland. The Cryosphere 18, 1753–1771. https://doi.org/10.5194/tc-18-1753-2024, 2024.

Martos, Y., Jordan, T., Catalán, M., Jordan, T., Bamber, J. & Vaughan, D. 2018: Geothermal heat flux reveals the Iceland hotspot track underneath Greenland, Geophysical Research Letters, 45, 8214–8222. https://doi.org/10.1029/2018GL078289, 2018.

Mavko, G., Mukerji, T. & Dvorkin, J. 2020: The rock physics handbook, 3rd edition, 727 pp. Cambridge: Cambridge University Press.

Mayborn, K.R. & Lesher, C.E. 2006: Origin and evolution of the Kangâmiut mafic dyke swarm, West Greenland. GEUS Bulletin 11, 61–86. https://doi.org/10.34194/geusb.v11.4917

McRoberts, E.C. & Morgenstern, N.R. 1974: The stability of thawing slopes. Canadian Geotechnical Journal 11, 447–469. https://doi.org/10.1139/t74-052

Mortensen, J., Engstrøm, F. & Lind, I. 1998: The relation among porosity, permeability, and specific surface of chalk from the Gorm Field, Danish North Sea. SPE Reservoir Evaluation & Engineering 1, 245–251. https://doi.org/10.2118/31062-PA

Nielsen, S.R., Skursch, O., Svennevig, K. & Ingeman-Nielsen, T. 2026: Shallow landslides in west Greenland – An emerging climate change-related geohazard. 37th Nordic Geological Winter meeting, Turku, Finland, 13/01/2026 - 15/01/2026.

Obu, J. *et al*. 2019: Northern Hemisphere permafrost map based on TTOP modelling for 2000–2016 at 1 km2 scale. Earth-Science Reviews 193, 299–316. https://doi.org/10.1016/j.earscirev.2019.04.023.

Orlander, T., Adamopoulou, E., Jerver Asmussen, J., Marczyński, A. A., Milsch, H., Pasquinelli, L. & Fabricius, I. L. 2018: Thermal conductivity of sandstones from Biot's coefficient. Geophysics 83(5), D173-D185. https://doi.org/10.1190/geo2017-0551.1

Penner, E. 1970: Frost heaving forces in Leda clay. Canadian Geotechnical Journal 1. 7, 8–16.

Proestakis, E., Christensen, H.F., Meireles, L.T., Storebø, E.M., Shamsolhodaei, A. & Orlander, T. 2024: Detection and picking of shear wave arrival for stiffness evaluation of highly porous chalk. Geophysical Prospecting 72, 733–751.

Rezvanbehbahani, S., Stearns, L., Kadivar, A., Walker, J. & van der Veen, C. 2017: Predicting the geothermal heat flux in Greenland: A machine learning approach. Geophysical Research Letters 44, 12271–12279. https://doi.org/10.1002/2017GL075661, 2017.

Salje, E.K.H., Safarik, D.J., Lashley, J.C., Groat, L.A. & Bismayer, U. 2011: Elastic softening of metamict titanite CaTiSiO5: Radiation damage and annealing. American Mineralogist 96, 1254–1261. https://doi.org/10.2138/am.2011.3747

Sattler, K., Keiler, M., Zischg, A. & Schrott, L. 2011: On the connection between debris flow activity and permafrost degradation: a case study from the Schnalstal, South Tyrolean Alps, Italy. Permafrost and Periglacial Processes 22, 254–265. https://doi.org/10.1002/ppp.730

Sears, F.W., Zemansky, M.W., Young, H.D. & Freedman, R.A. 1987: University physics, 7th edition, 352 pp. Reading, MA: Addison-Wesley.

Sørensen, K., Korstgård, J.A., Mengel, F. & Weng, W.L. 2025: The Kangâmiut dyke swarm in West Greenland: a new map and insights into their tectonic evolution. GEUS Bulletin 59. https://doi.org/10.34194/3cy30452

Strunk, A., Krüger, S., Jensen, J. F., Olsen, J. & Jessen, C. 2024: Two millennia of climate change, wildfires, and caribou hunting in west Greenland. The Holocene 34, 1025–1035. https://doi.org/10.1177/09596836241247301

Svennevig, K. *et al*. 2024: A rockslide-generated tsunami in a Greenland fjord rang Earth for 9 days. Science 385, 1196–1205. https://doi.org/10.1126/science.adm9247

Taylor, J.R., 1997: An introduction to error analysis, 2nd edition, 327 pp. Sausalito, CA: University Science Books.

Tsytovich, N.A. 1959: Principles of geocryology, Part II, Chap. III. National Research Council of Cananada Technical Translation 1239, 28–79.

van Gool, J.A.M., Connelly, J.N., Marker, M. & Mengel, F.C. 2002: The Nagssugtoqidian Orogen of West Greenland: tectonic evolution and regional correlations from a West Greenland perspective. Canadian Journal of Earth Sciences. 39, 665–686. https://doi.org/10.1139/e02-027

van Tatenhove, F.G.M. & Olesen, O.B. 1994: Ground temperature and related permafrost characteristics in West Greenland. Permafrost and Periglacial Processesses 5, 199–215. https://doi.org/10.1002/ppp.3430050402

Viani, C., Chiarle, M., Paranunzio, R.,n Merlone, A., Musacchio, C., Coppa, G. & Nigrelli, G. 2020: An integrated approach to investigate climate-driven rockfall occurrence in high alpine slopes: the Bessanese glacial basin, western Italian Alps. Journal of Mountain Science 17, 2591–2610. https://doi.org/10.1007/s11629-020-6216-y

Wang, Y., Xie, J.-H., Yang, W., Li, X., Abulaiti, Z., Zheng, S., Zhu, J. & Xu, K. 2025: Permafrost thawing under overlaying salt water. Science Advances 11, eadp2808. https:// doi.org/10.1126/sciadv.adp2808

Waples, D.W. & Waples, J.S. 2004: A review and evaluation of specific heat capacities of rocks, minerals, and subsurface fluids. Part 1: Minerals and Nonporous Rocks. Natural Resources Research 13, 97–122. https://doi.org/10.1023/B:NARR.0000032647.41046.e7

Westermann, S. *et al.* 2023: The CryoGrid community model (version 1.0) – a multi-physics toolbox for climate-driven simulations in the terrestrial cryosphere. Geoscientific Model Development 16, 2607–2647. https://doi.org/10.5194/gmd-16-2607-2023

White, W.M. 2013: Geochemistry, 660 pp. Chichester: John Wiley & Sons, Ltd.

Zastruzny, S.F., Sjöberg, Y., Jensen, K.H., Liu, Y. & Elberling, B. 2024: Impact of summer air temperature on water and solute transport on a permafrost-affected slope in West Greenland. Water Resources Research 60, e2023WR036147. https://doi.org/10.1029/2023WR036147

Zimmerman, M. & Haeberli, W. 1992: Climatic change and debris flow activity in high-mountain areas. A case study in the Swiss Alps. Catena Supplement (Giessen), 22, 59–72.